Fracture prediction for the 1980 El Asnam, Algeria earthquake via elastic dislocation modeling

David Healy

Department of Earth and Ocean Sciences, University of Liverpool, Liverpool, UK

Graham Yielding

Badleys, Lincolnshire, UK

Nick Kusznir

Department of Earth and Ocean Sciences, University of Liverpool, Liverpool, UK

Received 21 August 2003; revised 28 July 2004; accepted 16 September 2004; published 18 December 2004.

[1] Geomechanical models based on linear elasticity have been used to predict the mode and distribution of subseismic fractures around larger faults. These models can be tested against field observations of surface breaks (fractures) formed in the aftermath of large earthquakes. This paper presents forward models based on elastic dislocation theory of the deformation due to the M_s 7.3 earthquake at El Asnam, Algeria in 1980. Using fault parameters from previous geodetic studies to define a set of larger faults, our models calculate the deformation field in the surrounding rock volume. We compare predicted strain and stress fields with the surface deformation measured in the area following the 1980 earthquake. Using a combination of the redistributed elastic dislocation stress due to slip on the major faults and a small component of overburden stress, the models successfully predict normal faults and tensile fractures in the hanging wall of the reverse fault system. Orientations of the predicted faults vary along strike of the fault system, being parallel to the main reverse fault in the south but oblique to it along the central segment, agreeing with observed surface breaks. The results of our forward modeling are not sensitive to the magnitude or direction of a regional tectonic stress. The predicted fractures are controlled by the near-field, short-term redistributed stresses due to coseismic slip. The agreement between modeled and measured deformation patterns adds confidence in the use of elastic dislocation theory to accurately predict small faults generated by coseismic slip on large faults. *INDEX TERMS:* 8010 Structural Geology: Fractures and faults; 8020 Structural Geology: Mechanics; 8107 Tectonophysics: Continental neotectonics; 8123 Tectonophysics: Dynamics, seismotectonics; 8168 Tectonophysics: Stresses—general; *KEYWORDS:* earthquake, surface break, elastic dislocation, fracture prediction, geodetic, neotectonic. **Citation:** Healy, D., G. Yielding, and N. Kusznir (2004), Fracture prediction for the 1980 El Asnam, Algeria earthquake via elastic dislocation modeling, *Tectonics*, *23*, TC6005, doi:10.1029/2003TC001575.

0278-7407/04/2003TC001575$12.00

1. Introduction

[2] Forward fault displacement models based on elastic dislocation (ED) theory have been used to predict displacements and strains due to coseismic slip events [*King and Vita-Finzi*, 1981; *Stein and Barrientos*, 1985; *Stein et al.*, 1988]. More recently, ED forward modeling of faults resolved on reflection seismic profiles has been used to predict small-scale, subseismic fracture patterns in faulted hydrocarbon reservoirs [e.g., *Maerten et al.*, 2002; *Bourne and Willemse*, 2001; *Bourne et al.*, 2001]. In this paper, the strain fields from forward ED models are used to calculate a corresponding redistributed stress field associated with coseismic fault slip, which is then combined with regional stress and/or overburden stress components to define the total stress field within the faulted rock. This total stress field may be used to predict the mode, orientation and distribution of smaller, or "secondary," fractures, caused by the stress redistribution during faulting.

[3] The exposed surface deformation due to large onshore earthquakes can be used to test the predictions and constrain the parameters in elastic models. The M_s 7.3 El Asnam earthquake of October 1980 was one of the largest observed in the western Mediterranean region (Figure 1a). Several groups studied the immediate aftermath of this earthquake providing details on surface breaks [*Philip and Meghraoui*, 1983] and seismicity, including focal plane solutions of aftershocks in the surrounding area [*Yielding et al.*, 1981; *King and Yielding*, 1984]. From these data various authors have modeled the fault related displacements using elastic dislocation theory [e.g., *King and Vita-Finzi*, 1981; *Cisternas et al.*, 1982; *Ruegg et al.*, 1982; *Bezzeghoud et al.*, 1995]. Some of this earlier work relies on matching calculated vertical displacements against geodetic measurements made along a single benchmark route, but the general form of the deep slip is constrained

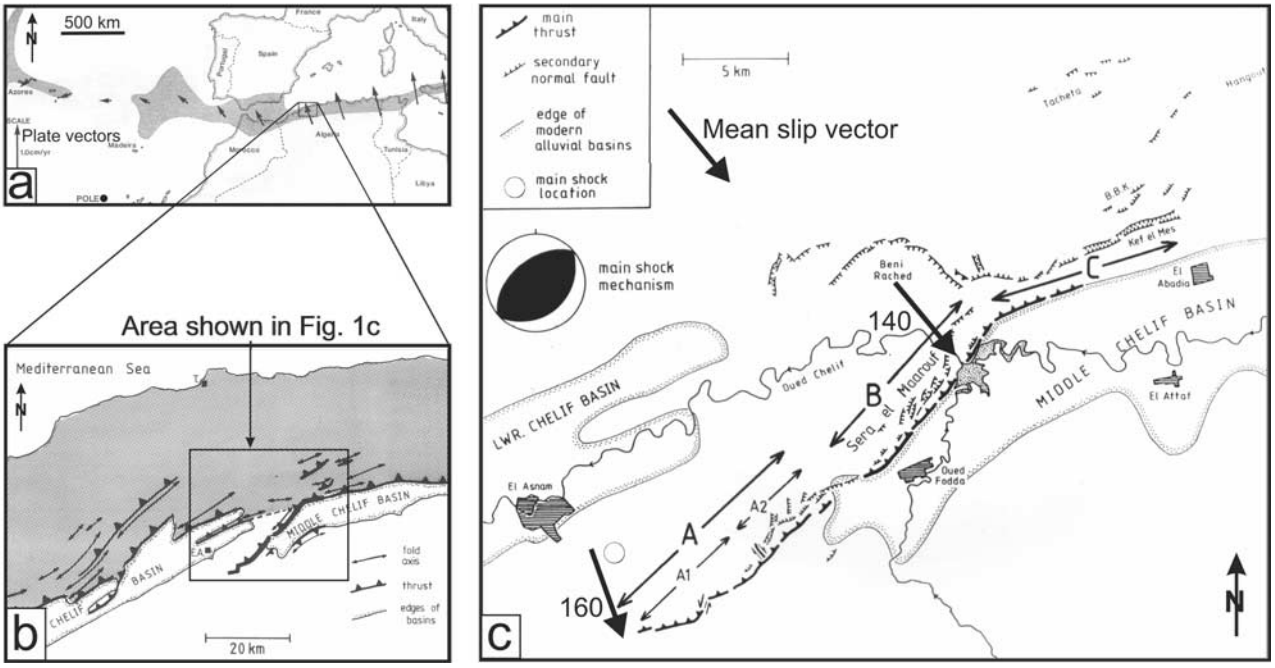

Figure 1. Location maps. (a) Map showing the broad area of active seismicity between North Africa and Europe with relative plate motion indicated by arrows [after *Anderson and Jackson*, 1987]. Overall convergence direction for Algeria is toward the NNW. Rectangle outlines the Chelif Basins. (b) Regional tectonic framework of the Lower and Middle Chelif Basins. Note the broadly NE/SW trending thrust faults and parallel fold axes. EA marks the location of the city of El Asnam. (c) Structural map [after *King and Yielding*, 1984] of the fault zone east of El Asnam. The main shock mechanism and location of the M_s = 7.3 earthquake on 10 October 1980 are indicated. A segmented reverse fault system over 30 km long trends NE/SW. In detail, a complex pattern of normal and strike-slip faults occurs in the hanging walls of the reverse faults. Tensile fractures are also abundant.

by analysis of a triangulated network by *Ruegg et al.* [1982].

[4] We present a new fault model for the 1980 earthquake at El Asnam that fits both the benchmarked geodetic data and the distribution of surface fractures. We compare modeled surface fracture patterns with those observed to further constrain the fault model. The geodetic data are limited to measurements of the vertical component of surface deformation; by using the surface fractures caused by the coseismic stress perturbation to constrain our models we can indirectly sample all three components of the near-surface displacement field. In addition, the surface fractures are spatially more widely distributed than the geodetic measurements.

2. El Asnam Earthquake of October 1980

2.1. General Setting

[5] Full details of the regional setting, earthquake seismology, aftershock distribution and surface deformation for the October 1980 El Asnam earthquake are given by *Yielding et al.* [1981], *Ruegg et al.* [1982], *Philip and Meghraoui* [1983], *King and Yielding* [1984], *Yielding et al.* [1989] and *Bezzeghoud et al.* [1995]. Here we simply describe the key features and some detailed structural observations used in testing the ED models.

[6] The city of El Asnam was located in the Algerian Atlas mountains (see Figure 1a) at the eastern end of the Lower Chelif Basin (the city was renamed Ech Chelif after the 1980 earthquake). Miocene-Pliocene marls, sandstones and calcarenites have been deformed by repeated tectonic activity. The area is dominated by NE trending reverse faults and associated hanging wall anticlines (Figure 1b). The 1980 earthquake occurred on a previously unrecognised, segmented reverse fault with a surface rupture running for a total of 30 km (Figure 1c). The average fault trace trends around 050° and the average fault slip direction was around 140°. Field measurements on exposed fault planes reveal no significant strike-slip component at the surface. Focal plane solutions for the main shocks are consistent with the observed reverse fault geometry, and the aftershock distribution is consistent with a planar fault system extending to at least 10 km depth.

2.2. Key Structural Features

[7] An important observation from the detailed structural mapping is the wide range of smaller faults developed around the larger reverse faults. Fractures with normal, strike-slip and reverse displacements, and oblique-slip combinations and tensile fissures are present in complex networks (for details see *Yielding et al.* [1981] and *Philip and*

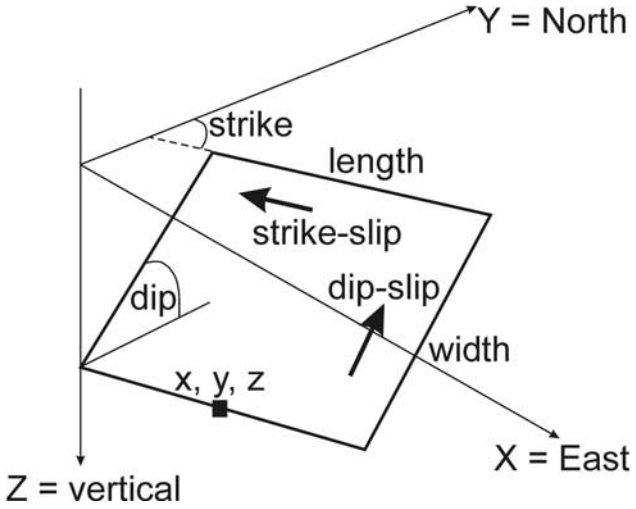

Figure 2. Diagram to illustrate the configuration of a simple elastic dislocation (ED) model, according to the formulation of *Okada* [1992]. Calculations are performed on a regular grid of observation points for a specified surface through the half-space. Faults are modeled as rectangular panels with horizontal upper and lower edges. Slip values are prescribed for each fault panel.

Meghraoui [1983]). In the north central segment around Sera el Maarouf (labelled B on Figure 1c), a prominent asymmetric anticline forms a topographic ridge in the hanging wall of a reverse fault. An en echelon zone of normal faults with linking arrays of tensile fissures is developed along the crest of this ridge. The normal fault planes trend NNE/SSW, oblique to the underlying reverse fault. Measurements of fault offset, taken shortly after the 1980 earthquake [*King and Vita-Finzi*, 1981; *Yielding et al.*, 1981], indicate slip vectors normal to the underlying reverse fault trace. Fault plane slickenlines recorded from shear fractures exposed in this area [*Philip and Meghraoui*, 1983] must have existed prior to the 1980 event, because mechanical considerations dictate that surface fractures are tensile. Along the south central segment (labelled A2 on Figure 1c) normal faults and tensile cracks are present in another hanging wall anticline, but these extensional fractures run parallel to the underlying reverse fault. At the SW tip of exposed surface breaks there is some evidence from fault striae for a small (1–2 m) sinistral component of fault slip. These observations are supported by focal plane solutions for numerous aftershocks measured in the area (see Figure 8 of *King and Yielding* [1984]).

3. Formulation of the Elastic Dislocation Fracture Prediction Model

3.1. Elastic Dislocation Theory

[8] In ED theory [*Steketee*, 1958; *Rongved and Frasier*, 1958] faults are considered as displacement discontinuities or dislocations in an otherwise continuous elastic medium. Faults are represented as surfaces across which there is defined to be a discontinuity in the elastic displacement field. The surrounding volume is modeled as a uniform elastic half-space with boundary conditions of zero normal and shear tractions at the free surface and zero displacement at an infinite distance from any dislocation (i.e., a fault). ED theory is conceptually valid for modeling coseismic deformation. If fault slip values are small relative to fault length/width (<1–2%), the resulting displacements and strains are effectively infinitesimal. The ED formulation of *Okada* [1985, 1992] is used in our models, which expresses the displacement field $\mathbf{u}_{x,y,z}$ at any given point as a function of fault parameters (slip, dip, strike, length, and width) and the elastic constants within the continuum, for rectangular fault panels with horizontal upper and lower edges (Figure 2). The Okada formulation is mathematically robust and tractable, and these attributes make it suitable for rapid, iterative, forward numerical modeling. For modeling the El Asnam earthquake, an array of rectangular panels is a sufficient approximation to the true fault geometry given the sparse constraints at depth. The restrictions within the Okada ED formulation to an elastic half-space and to rectangular fault panels with horizontal upper and lower edges have no significant effect on our model results. Singularities of calculated displacement and strain can result from observation points located at the edges of fault panels but such problematic points are systematically distributed and can be removed.

3.2. Model Configuration and Parameters

[9] The elastic constants and other mechanical parameters used throughout this study are shown in Table 1. We are investigating the coseismic response of the rocks and therefore we model the continuum as a purely elastic solid with no viscous effects (Poisson's ratio $\nu = 0.25$). Figure 2 illustrates the configuration of a simple ED fault model with a fault plane represented as a rectangular panel with separate prescribed slip values for strike slip and dip slip. Displacements and strains are calculated at discrete observation points, defined as a regular grid on a specified surface. The coordinate reference frame used in this work is also shown.

Table 1. Values of Material Parameters Used in This Study (Unless Otherwise Stated)

Parameter	Value
Gravitational acceleration, g	9.81 m s^{-2}
Density, ρ	2000 kg m^{-3}
Poisson's ratio, ν	0.25
Young's modulus of basement, E_b	50 GPa
Lamé's constant of basement, λ_b	20 GPa
Shear modulus of basement, G_b	20 GPa
Young's modulus of sediment, E_s	5 GPa
Lamé's constant of sediment, λ_s	2 GPa
Shear modulus of sediment, G_s	2 GPa
Coefficient of internal friction, μ_i	0.6
Tensile strength, T_0	0.5 MPa
Cohesion (shear strength), C	1 MPa

3.3. Calculation of Displacement, Strain, and Stress

[10] Vertical displacements ($\mathbf{u}_z$ component of the elastic displacement field), in metres, have been calculated for grid nodes at the surface (z = 0 m). All models use the same grid node array with a uniform 0.5 km horizontal spacing between nodes. The full elastic strain tensor is also calculated using the same grid node array and is used to calculate an elastic stress tensor for each grid node using Hooke's Law:

$$\sigma_{ij} = 2G\varepsilon_{ij} + \lambda\varepsilon_{kk}\delta_{ij}, \quad (1)$$

where σ_{ij} is the elastic stress tensor, G is the shear (or rigidity) modulus, ε_{ij} is the elastic strain tensor, λ is the Lamé constant, and δ_{ij} is the Kronecker delta. The strain and stress fields derived from ED theory represent the elastically redistributed deformation due to slip on the faults.

[11] In order to predict rock fracture arising from a coseismic stress redistribution, we need to consider the total stress field including overburden stresses (for grid nodes below the surface, z > 0) and the tectonic or regional stress. For the overburden stress components we assume

$$\sigma_{xx} = \sigma_{yy} = \sigma_{zz} = \rho g z, \quad (2)$$

where ρ is the density of the overburden (assumed constant), g is acceleration due to gravity and z is the depth. This condition corresponds to a hydrostatic state of stress for the lithostatic overburden component, implying that the overburden has no long term shear strength. We believe this to be a valid approximation for fractured and weathered near-surface rocks, such as those present around the El Asnam fault system, where stress corrosion acts on the joints and fissures [*King and Vita-Finzi*, 1981; *Vita-Finzi and King*, 1985]. Note that this does not contradict the use of an elastic model to calculate stress changes induced by abrupt fault slip over a period of some 30 seconds. Using equation 2 and the values for g and ρ listed in Table 1, the vertical component of overburden stress at 50 m depth will be approximately 1 MPa, rising to 2 MPa at 100 m depth. Given the relatively low strength of the exposed rocks (cohesion estimated at 1 MPa, see Table 1), this overburden component of stress is likely to be significant. The apparently low value of cohesion used in our model is based on field observations and the assumption that repeated earthquakes in the region combined with near-surface weathering will have weakened the initially intact rock mass to a much lower strength. The local topography is cut by gorges between 50–100 m deep. Note that the low cohesive strength we have chosen for these surface rocks (1 MPa, Table 1) is still sufficient to maintain the maximum shear stress induced by the overburden alone ($\sim$1 MPa), and therefore maintain this amount of topographic relief.

[12] To calculate the regional or tectonic stresses we use estimates of regional strain. *Ruegg et al.* [1982] used a triangulation network around the fault system to estimate the strain tensor associated with the 1980 earthquake; their results can be summarised as a uniaxial shortening of 2.0×10^{-4} along a direction of 140°. From this simplistic strain field with principal strains $\varepsilon_1 = 2 \times 10^{-4}$ and $\varepsilon_2 = \varepsilon_3 = 0$, we apply Hooke's Law to derive corresponding regional principal stresses of σ_1 = 1.2 MPa (most compressive), σ_2 = 0.4 MPa and σ_3 = 0 MPa (least compressive). Assuming linear isotropic elasticity, σ_1 is horizontal and aligned parallel to ε_1 along 140°, σ_2 also horizontal, aligned 050° and σ_3 is vertical. This regional stress field gives a maximum regional shear stress of 0.6 MPa, which is significant in its magnitude. The presence of faulted rock does not necessarily imply that the total stress must have exceeded the failure strength at the time of slip [*Bourne and Willemse*, 2001], only that it must have exceeded the failure strength at some time in the past. Imposed total stresses below the failure strength could reactivate favorably oriented preexisting faults and the large reverse faults around El Asnam were certainly in existence before the 1980 event [*King and Vita-Finzi*, 1981]. In modeling the surface and near-surface deformation around El Asnam we have chosen to ignore pore-fluid pressure in the stress calculations. This maximises the effective stresses, and therefore minimises potential for failure; including pore-pressure would generate more fracturing, but not change its orientation (see also later discussion).

4. Results From Forward Elastic Dislocation Modeling of the 1980 El Asnam Earthquake

[13] Forward modeling attempts to find a best fit to observed data by a process of trial and error, and model solutions are necessarily nonunique. To assess comparable forward ED models of the coseismic deformation at El Asnam, we employ a combination of quantitative data and more qualitative evidence. Three forward ED models are presented in this paper and their results are compared. Table 2 lists the fault parameters of each model. The fault panel outlines and the fault surface traces for all three models are shown in Figure 3.

[14] Model 1 is taken from *Ruegg et al.* [1982] (their Model 03) and comprises a set of four fault panels (see Figure 3a) with varying orientations and a mixture of reverse dip-slip and sinistral strike-slip. Note that although *Ruegg et al.* [1982] presented the results from a "better" five-panel model, no parameters were listed for the fifth panel: as such we were unable to model this configuration. Model 2 is taken directly from *Bezzeghoud et al.* [1995] (their model G) and involves ten panels segmented in a downdip direction into a ramp-flat-ramp geometry (Figure 3c), all with reverse dip slip only. There is no panel in this model to represent the fault breaks and deformation in the NE corner of the area. Model 3 represents our preferred model and is derived largely from that of *Ruegg et al.* [1982] (i.e., Model 1). However, we segment the central panels downdip (Figure 3e) with the middle panel in each central segment carrying a larger reverse dip-slip value. Note that none of the panels in our initial model have a strike-slip component. The total geometric moment of Model 3 amounts to 2.0×10^9 m^3, and using a value for shear rigidity appropriate to basement rocks G_b (see Table 1), this corresponds to a seismic moment of approx-

Table 2. Fault Panel Data for the Three Models in This Study[a]

	UTM Coordinates (Zone 31), km			Dimensions, km		Orientation, deg		Fault Slip, m	
Panel	X	Y	Z	L	W	Dip	Strike	Sinistral	Reverse
				Model 1					
1	353.19	4001.46	11.28	10.0	10.0	70.0	057.5	1.0	1.0
2	357.03	4007.12	11.26	6.0	12.5	60.0	044.1	2.0	3.0
3	362.60	4015.03	12.14	10.0	14.9	54.0	040.5	1.0	8.0
4	375.56	4024.12	12.14	8.0	13.0	54.0	067.0	0.0	3.0
				Model 2					
1	360.44	4009.05	9.76	21.0	5.15	67.5	037	0.0	8.0
2	356.52	4000.43	4.95	2.5	1.35	67.5	037	0.0	4.0
3	356.93	4000.12	3.70	2.5	4.00	67.5	037	0.0	1.5
4	359.09	4003.93	5.04	6.2	1.78	60.0	037	0.0	4.0
5	359.80	4003.39	3.46	6.2	4.00	60.0	037	0.0	1.0
6	361.45	4007.69	4.98	2.7	6.20	53.5	037	0.0	8.0
7	365.42	4012.50	4.95	9.5	4.00	30.0	037	0.0	8.0
8	368.18	4010.41	2.12	9.5	1.00	60.0	037	0.0	5.0
9	368.58	4010.11	1.41	9.5	1.00	60.0	037	0.0	3.0
10	368.98	4009.81	0.71	9.5	1.00	60.0	037	0.0	2.0
				Model 3a					
1	353.33	4003.99	8.09	5.0	10.00	54.0	063	0.0	4.0
2a	357.77	4007.33	8.49	8.0	4.25	54.0	050	0.0	6.5
2b	359.37	4005.41	5.06	8.0	5.50	54.0	050	0.0	9.0
2c	361.45	4002.94	0.61	8.0	0.75	54.0	050	0.0	1.0
3a	363.58	4014.05	7.07	11.0	4.00	45.0	040	0.0	5.5
3b	365.75	4012.23	4.24	11.0	5.00	45.0	040	0.0	12.0
3c	368.46	4009.95	0.71	11.0	1.00	45.0	040	0.0	0.6
4	373.88	4023.70	7.72	8.0	10.00	40.0	070	0.0	3.0

[a]Panel coordinates refer to the midpoint of the lower panel edge [see *Okada*, 1992]. Panels for Model 1 are derived from data of *Ruegg et al.* [1982]. Fault slips involve a mixture of sinistral and reverse components. Fault panels for Model 2 are derived from data of *Bezzeghoud et al.* [1995]. Note that these panels only carry reverse dip slip. Fault panels for our initial Model 3a are from this study.

imately 4.0×10^{26} dyne cm. These values are in close agreement with the geodetic estimate of *Ruegg et al.* [1982] and the seismic estimates by *Yielding* [1985], *Deschamps et al.* [1982] and *Brustle and Muller* [1983].

4.1. Vertical Surface Displacements Due to Coseismic Slip

[15] Geodetic data have been collected by *Ruegg et al.* [1982] and *Bezzeghoud et al.* [1995]. In this paper, we use the geodetic measurements made during the 1986 campaign of *Bezzeghoud et al.* [1995] which provides vertical displacements along a single route of 25 benchmarks. Much of this route (see symbols on fault panel maps in Figure 3) runs subparallel to the main fault strike with only a short segment (benchmarks 10–16) normal to fault strike. In our forward modeling, greater weight has been given to the fit of modeled displacement values to those benchmarks closer to the fault and trending normal to fault strike, compared to those further away. The benchmarked route represents an oblique one-dimensional transect through the central segment. More qualitative information for the whole area is available from detailed local knowledge of the neotectonic features and surrounding topography on the assumption that repeated occurrences of earthquakes similar to that of 1980 have created the observed structures.

[16] Figures 3b, 3d, and 3f show contour maps of predicted vertical displacements ($\mathbf{u}_z$) for each of the three fault models, and Figure 4 shows corresponding graphs of calculated versus observed vertical displacement along the benchmark route. Figure 3b shows that Model 1 produces significant uplift in the immediate hanging walls of the central and northeasterly segments matching the observations of topographic ridges and anticlines in these areas. The fit to the geodetic data (Figure 4a) is imperfect especially around the key central benchmarks (10–16). The overall form of the predicted vertical displacements appears valid but the hanging wall has insufficient uplift and the footwall has too much subsidence. *Ruegg et al.* [1982] noted that their model required an extra short fault segment between their panels 2 and 3.

[17] While not including the northeast segment of the fault zone, Model 2 also manages to produce a prominent uplift in the hanging wall of the north central segment (Figure 3d). However, this displacement high does not coincide with the Sera el Maarouf anticlinal ridge, which is situated closer to the main reverse fault trace. The overall fit to the geodetic data shows an apparent improvement over that in Model 1 (compare Figure 4a with Figure 4b). The calculated vertical displacements around the central benchmarks are higher than in Model 1. However, close inspection of the map in Figure 3d and the panel configuration shown in Table 2 for Model 2 data shows that this fit to the benchmark data is due to the extremely high slip values on panel 6. This produces a vertical displacement high in an area where, on the ground, there is a prominent gap between two offset

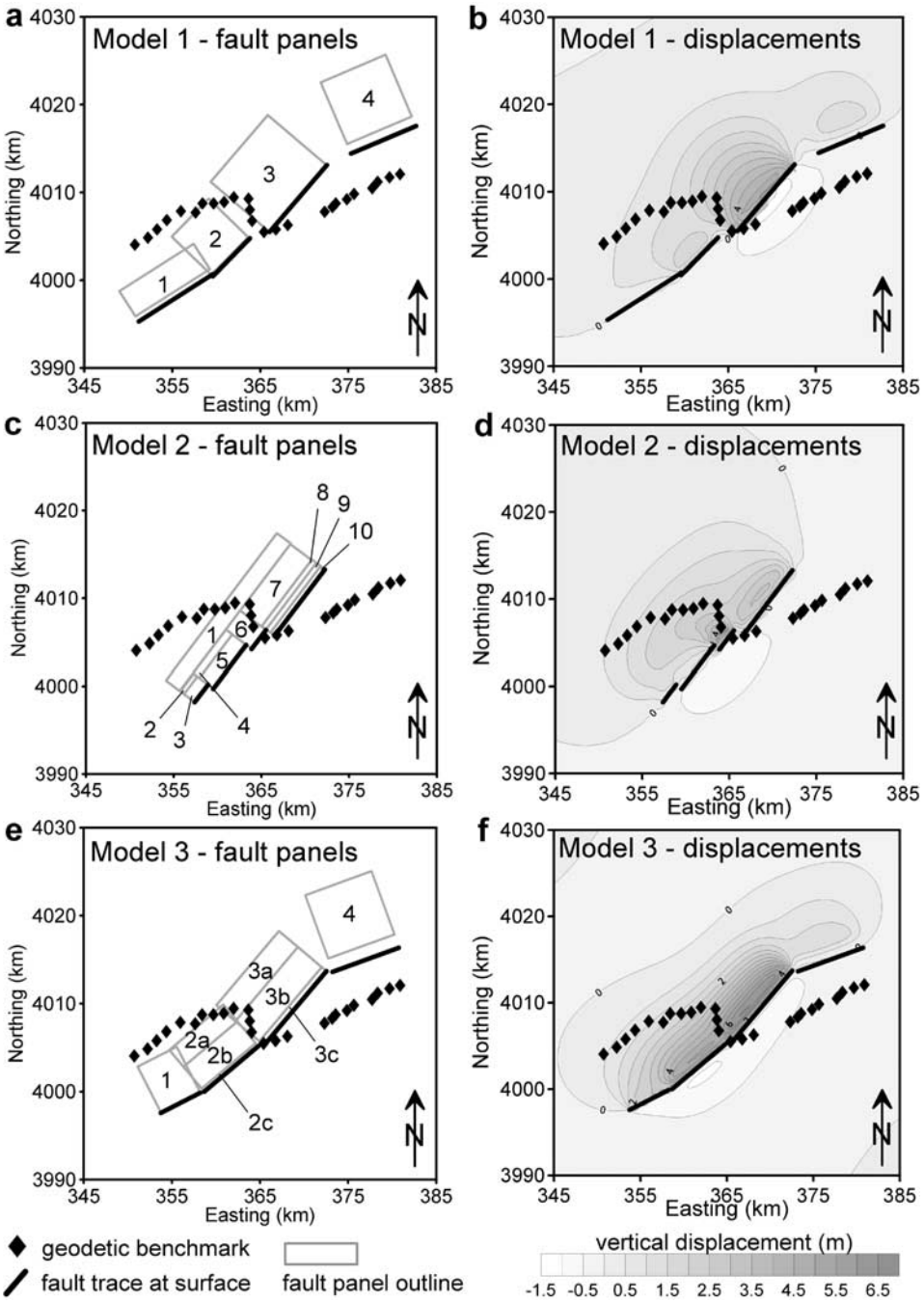

Figure 3. (a–f) Maps of subsurface fault panels and calculated vertical displacement ($\mathbf{u}_z$ component of elastic displacement field) for each of the three models presented in this study. The numbers on the fault panels refer to the panel numbers listed in Table 2. The locations of the geodetic benchmarks used in the 1986 campaign [after *Bezzeghoud et al.*, 1995] are shown as rhombs. Maps of vertical displacement are contoured in meters. Model 1 fails to produce significant uplift in the hanging wall of panel 2. Model 2 predicts an isolated high of vertical displacement where the benchmark route cuts the fault zone, yet this is not matched by observations. Model 3a predicts elongate zones of uplift in the immediate hanging walls of the central fault panels, with a slightly less uplifted zone in between along the benchmark route; this model provides the closest fit to the observations. Map projection for these, and all subsequent maps, is UTM (zone 31) with coordinates in kilometers.

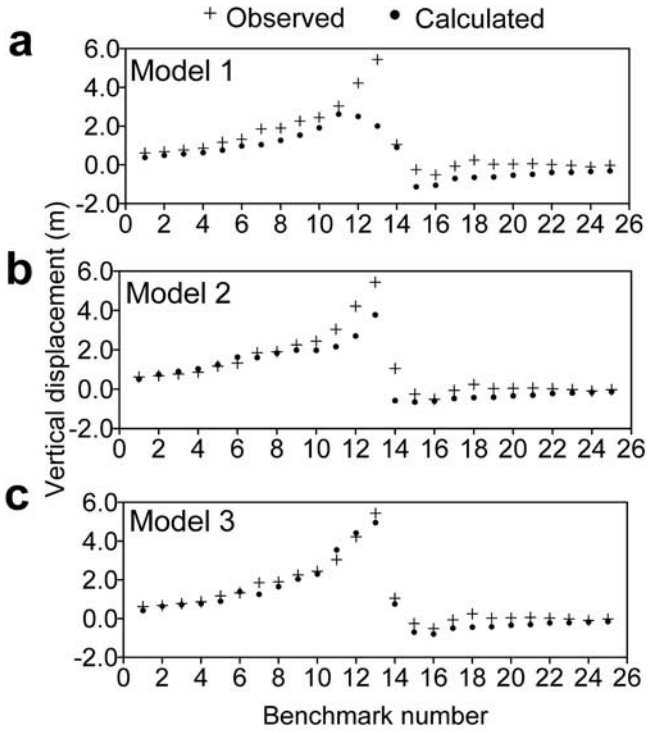

Figure 4. (a–c) Graphs of observed (crosses) versus calculated (dots) vertical displacements for each of the three models of Figure 3. Observations were made along 25 geodetic benchmarks (see maps in Figure 3). All values are simply plotted for each benchmark along the route with no allowance for actual distance along the ground and these graphs should not be considered as a true profile through the fault zone.

topographic ridges (the benchmark route follows a road and railway line through this gap).

[18] The vertical displacements calculated from Model 3a are shown in Figures 3f and 4c. Displacement highs are present in the hanging walls of the main fault panels and lie close to the fault traces, matching the occurrence of hanging wall uplift in these areas. These highs result from increased slip on deeper panels combined with a sudden decrease in slip on the shallowest panels. A saddle in the predicted vertical displacement field is present along the central portion of the benchmark route, in contrast to Model 2. The fit to the geodetic data is also good (Figure 4c), particularly along the central benchmarks and predicted lack of footwall subsidence toward the NE.

4.2. Elastic Dislocation Strains Due to Coseismic Slip

[19] In addition to the displacement field, ED models calculate the full strain tensor at each grid node. The volumetric strain, or dilatation, Δ is defined as

$$\Delta = \varepsilon_1 + \varepsilon_2 + \varepsilon_3, \quad (3)$$

where ε_1, ε_2, ε_3 are the principal strains calculated as eigenvalues of the symmetric part of the elastic strain tensor. Large positive values of Δ represent significant volume gain, and large negative values correspond to significant volume loss. Areas of extreme volumetric strain can be considered as more highly deformed and possibly therefore as more likely to be intensely fractured. Figure 5 shows the contoured values of elastic volumetric strain for Models 1, 2 and 3.

[20] Models 1 and 3 both predict high dilatation (positive Δ) in the immediate hanging walls of the main reverse fault panels. These regions correspond to areas of extensional normal faulting and tensile fissures which is consistent with the predictions. The linear form of these extended/tensile zones trending NE/SW parallel and close ($\sim$1 km) to the reverse faults more closely matches the predictions of Model 3. Model 2 predicts high values of Δ in the central gap area (panel 6 on Figure 3c). On the ground, this area is covered by alluvium and some strain may be concealed beneath these recent sediments.

[21] On the basis of our assessment of the fit between modeled and observed vertical displacements and volumetric strain, subsequent model results are shown only for our preferred Model 3. The orientation of the ED strain field produced by Model 3 is shown in Figure 6 for a depth of 50 m. Note that throughout this paper our convention for strains is $\varepsilon_1 > \varepsilon_2 > \varepsilon_3$ with elongation reckoned as positive, and shortening as negative. In these maps, the orientations of the ε_1 and ε_3 principal strains are depicted with a line symbol, where the direction of the line represents the azimuth of the strain axis and the length of the line is inversely related to the plunge of the strain axis. A line of zero length therefore represents a vertical strain axis. Note therefore that the lengths of the lines carry no indication of strain magnitude or sign. The background to each strain map shows the volumetric strain. In Figure 6a, the maximum principal strain (ε_1) is approximately horizontal and normal to the main fault traces along the linear high strain zones in the hanging walls. In Figure 6b we can see that at these locations the minimum principal strain (ε_3) is subvertical. These maps show that although the ED strain field around the fault panels is heterogeneous, there are systematic transitions between domains of different strain orientation.

4.3. Redistributed Stress, Overburden Stress, and Regional Stress

[22] Assuming linear elasticity in an isotropic medium we can derive the ED stress field from the ED strain field using Hooke's Law, equation (1). To calculate the redistributed elastic stress field in the near-surface rocks due to a coseismic slip increment within the underlying basement, we use values for the shear rigidity G_s and for the Lamé constant λ_s (see Table 1) appropriate to fractured and chemically weathered rocks. The orientations of the modeled principal ED stresses will match those of the principal ED strains. The convention for stresses is $\sigma_1 > \sigma_2 > \sigma_3$ with compression reckoned as positive and tension as negative. For the ED deformation field, ε_3 (minimum principal strain) corresponds to σ_1

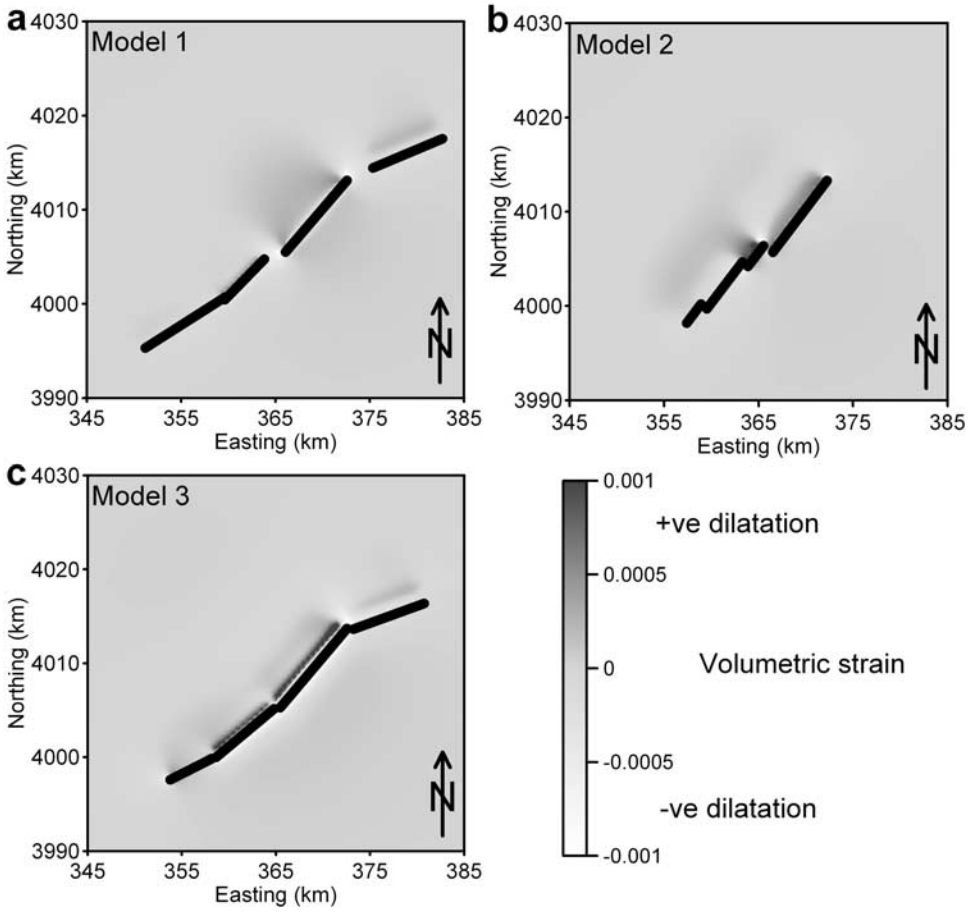

Figure 5. Maps of volumetric strain for the ED component of the deformation for each of the three models. Volumetric strain contours are capped at ±0.001 and are computed for a depth 50 m below the free surface. Note the linear zone of predicted positive dilatation along the hanging wall of the central fault segments in Model 3a.

(maximum principal stress) and ε_1 (maximum principal strain) corresponds to σ_3 (minimum principal stress).

[23] The maximum Coulomb shear stress, MCSS [*Jaeger and Cook*, 1979] is defined as

$$MCSS = \left[\tau_{max} \cdot \sqrt{\left(1+\mu^2\right)} - \left(\mu \cdot \sigma_{mean}\right)\right], \qquad (4)$$

where τ_{max} is the maximum shear stress ($[\sigma_1 - \sigma_3]/2$), σ_{mean} is the mean stress ($[\sigma_1 + \sigma_3]/2$), and μ is the coefficient of internal friction (see Table 1). We choose to normalise calculated MCSS values by the shear strength (C) of the rock. Then for a given stress state, the value of normalised MCSS reflects how far the rock is from its shear strength (cohesion); this is illustrated in Figure 7. Values of normalised MCSS greater than 1 imply that the rock has failed and regions of extremely high normalised MCSS are expected to be intensely fractured.

[24] The orientations of σ_1 and σ_2 for the ED stress field at a depth of 50 m, resulting from Model 3, is depicted in Figure 8. The correspondence between the orientation of σ_1 and ε_3 can be seen by comparing Figure 8a with Figure 6b. Similarly, the regions of high normalised MCSS roughly correspond to the areas of extreme volumetric strain with linear zones in the hanging walls of the panels in the central segment. The most compressive principal stress σ_1 is subvertical in these high MCSS zones. In the high MCSS zones, σ_2 is oriented approximately horizontal and parallel to the fault panel traces (Figure 8b). In the Andersonian fault model [*Anderson*, 1951], the relative orientations of the principal stress directions with respect to the free surface control the type of faulting. Normal faults result from σ_1 vertical and σ_2 and σ_3 horizontal. Strike-slip faults result from σ_1 and σ_3 horizontal with σ_2 vertical. In addition, the orientation of σ_2 indicates the direction along which conjugate shear failure planes intersect. Using a simple Andersonian scheme of fault classification, the ED stress field of Model 3a is consistent with normal faults and/or tensile fractures in the immediate hanging walls of, and striking parallel to, the central fault panels.

[25] Some of the minor fractures around El Asnam are observed to penetrate to depths of 50 m–100 m in gorges

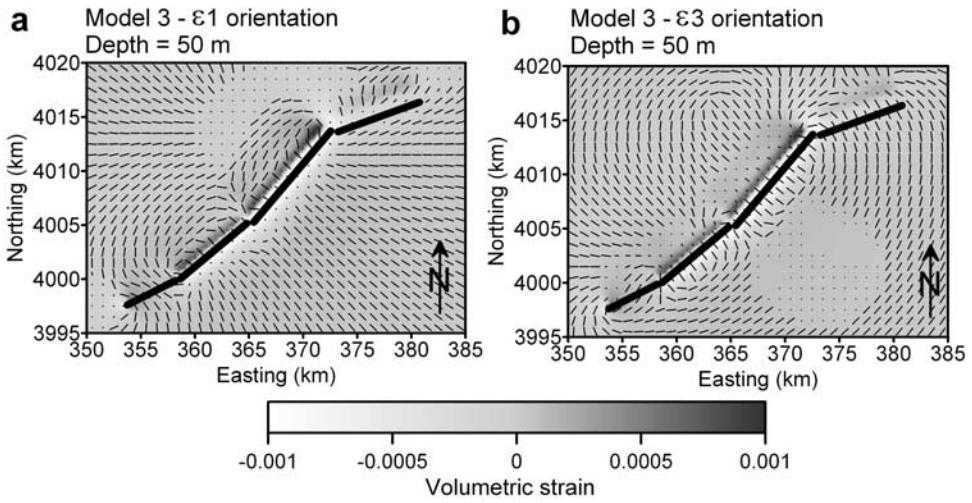

Figure 6. Maps of ED strains in the subsurface; z = 50 m. (a) Orientations of ε_1 principal strain on a background of volumetric strain. (b) Orientations of ε_3 principal strain on a background of volumetric strain.

cutting through the topography created by the hanging wall anticlines. Therefore, in modeling the stress field responsible for the observed fractures we need to consider the load due to overburden. Since the model is based on linear elasticity, we superpose the ED stress with a lithostatic overburden stress as described above. Figures 8c and 8d show this combined stress field at a depth of 50 m. The normalised MCSS values tend to drop slightly (compare the extent of grey areas on Figures 8c–8d with those on Figures 8a–8b) because the mean stress is higher. This would imply less intense fracturing with depth.

[26] In modeling the total stress field controlling fracture formation, a regional or tectonic stress component needs to be considered. As described above, we use regional strain values from *Ruegg et al.* [1982] to estimate the orientation and magnitude of this regional component to the total deformation. Figures 8e–8f show a total stress field calculated by the linear superposition of ED, overburden (50 m) and regional stresses. The far-field (i.e., away from the defined fault panels) is dominated by the regional stress component, as the ED stress component weakens significantly away from the main faults. In the near-field, the elastic stress perturbation to the regional stress field is apparent. The regional far-field stress is clearly consistent with an overall reverse/thrust fault in the Andersonian sense, but the elastic perturbations to the total field around the larger faults will modify the orientation and type of smaller scale faulting. The linear zones of high MCSS are still present in the hanging walls of the central segment coincident with steep to subvertical σ_1 and subhorizontal NE striking σ_2. The regional and ED stress (strain) components tend to be of opposite sign, especially around the fault panels. The area around the fault therefore experiences net stress (strain) relief; however, the ED strains in Model 3a associated with the upper tip line are locally very high where the displacement on the panels falls of quite rapidly toward the surface. These locally high ED strains dominate over the regional strains and cause the high values in MCSS. The addition of the regional compressive stress field does not affect the predicted distribution of extensional structures in the near-field around the faults, particularly in the hanging walls of the central fault segments.

[27] The systematic modeling of the various stress components allows us to assess their contribution to the

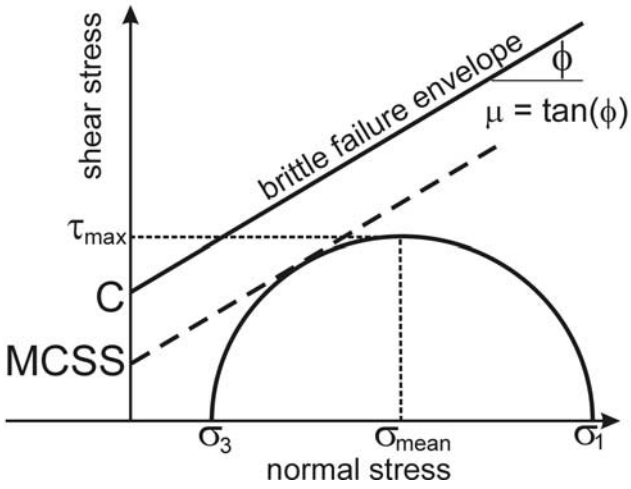

Figure 7. Cartoon Mohr diagram illustrating the relationship between maximum Coulomb shear stress (MCSS) and the cohesion (or shear strength) *C*. MCSS represents the intercept on the shear stress axis of the tangent to the Mohr circle that is parallel to the failure envelope. A normalized MCSS value greater than 1 for a given point implies the rock mass has exceeded its shear strength.

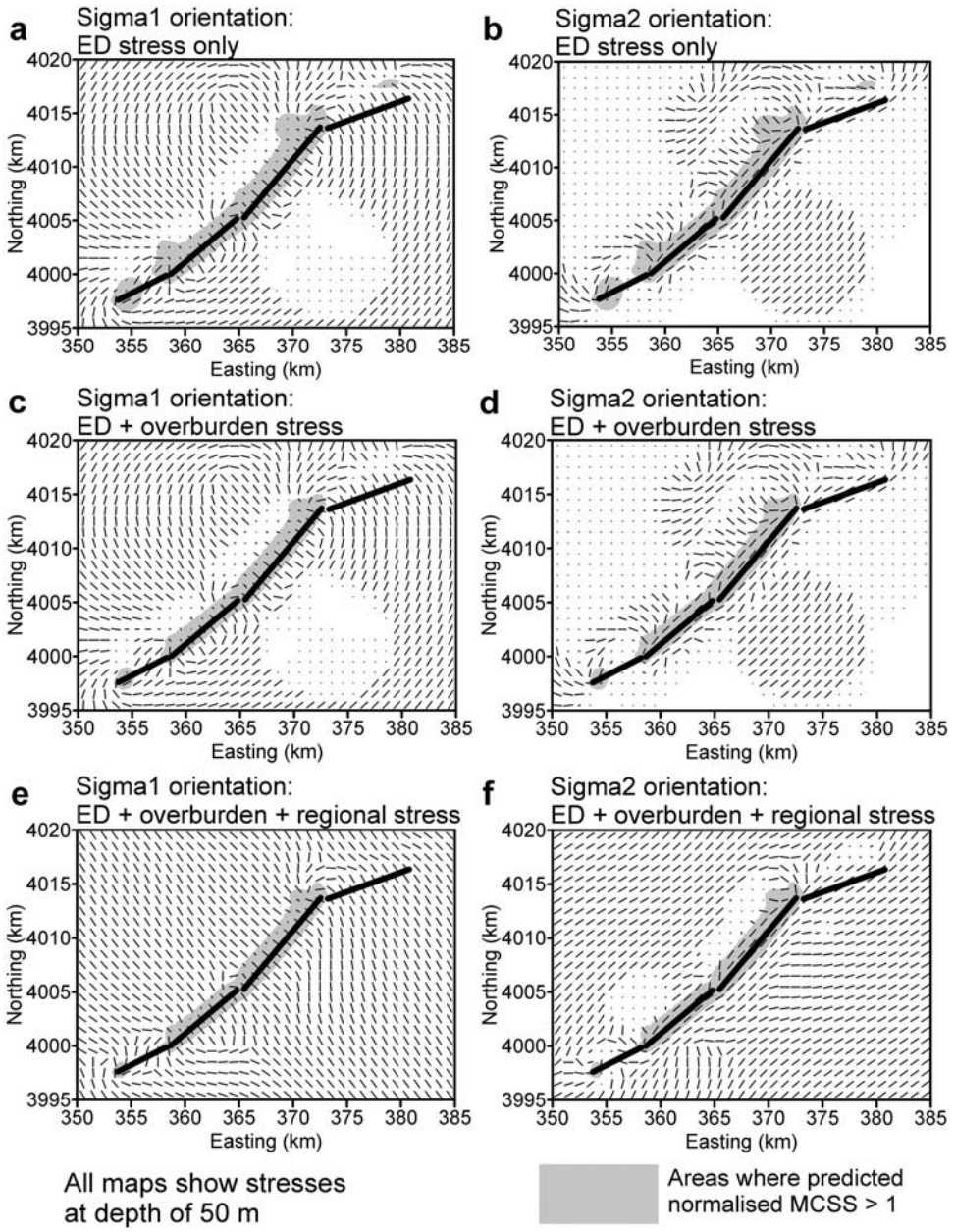

Figure 8. Maps of stresses in the subsurface; z = 50 m. (a) Orientation of σ_1 principal stress (most compressive) for the ED component of the deformation on a background of normalised maximum Coulomb shear stress. (b) Orientations of σ_2 principal stress (intermediate) for the ED component of the deformation on a background of normalised maximum Coulomb shear stress. (c) Map of ED + overburden stresses in the subsurface, z = 50 m. Orientations of σ_1 principal stress (most compressive) on a background of normalised maximum Coulomb shear stress. (d) Orientations of σ_2 principal stress (intermediate) on a background of normalised maximum Coulomb shear stress. (e) Map of ED + overburden + regional stresses in the subsurface; z = 50 m. Orientations of σ_1 principal stress (most compressive) on a background of normalised maximum Coulomb shear stress. (f) Orientations of σ_2 principal stress (intermediate) on a background of normalised maximum Coulomb shear stress.

observed deformation. The stress field due to the combination of ED and overburden alone is sufficient to account for the mapped structures (compare Figures 8c–8d with Figures 8e–8f) and the regional stress component exerts no obvious control on the formation of smaller scale fractures. Fractured and weathered near-surface rocks probably do not sustain regional stresses i.e., they possess no long-term shear strength. An applied regional stress (e.g., from far-field plate convergence) will be slowly dissipated at shallow levels due to slip on

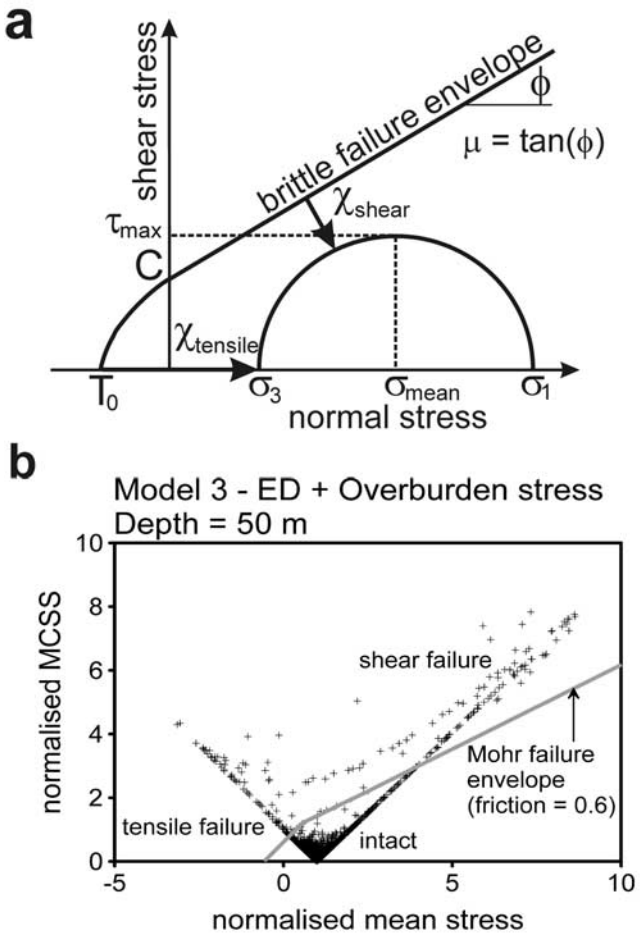

Figure 9. (a) Graph illustrating the concept of proximity to failure for both tensile ($\chi_{tensile}$) and shear (χ_{shear}) modes. The proximity to failure method of *Bourne and Willemse* [2001] is used to determine the failure mode at each grid node. (b) Predicted ED + overburden stress states for our preferred Model 3, calculated at a depth of 50 m. Note that many points exceed the example failure envelope, calculated with a coefficient of internal friction μ_i = 0.6. Maximum shear stresses and mean stresses have been normalised by the cohesive strength (1 MPa).

preexisting fractures and chemical processes [*King and Vita-Finzi*, 1981; *Vita-Finzi and King*, 1985]. Therefore, at the time of the 1980 earthquake, the load on the near-surface rocks would only have been due to the stresses arising from the short-term elastic response to the coseismic slip (modeled by the ED stress component) and the weight of any overlying rock (modeled by the lithostatic overburden stress). Our models suggest that this simple stress field can successfully account for the distribution and mode of the observed fractures e.g., Figures 8c–8d. Specifically, an extensional regime is predicted for the narrow linear zones along the hanging walls of the central faults matching the observed normal faulting and tensile fracturing in these areas. However, a failing of the current model (Model 3a) is that the NNE trending (i.e., oblique) normal faults in the hanging wall anticline along Sera el Maarouf are not predicted. The orientation of σ_2 in our model of this region is parallel to the main reverse fault trace, and predicted fractures would therefore strike NE. We address this issue later (see below).

4.4. Predicted Fractures Due to Redistributed and Overburden Stress

[28] In order to predict fractures, we seek a model that can account for their distribution, mode and orientation. The distribution is likely to be controlled by stress magnitude and our maps depict fractured areas as those where the normalised maximum Coulomb shear stress exceeds 1. The next task is to identify the mode of failure, tensile or shear, before applying a particular failure criterion to calculate failure plane orientation [e.g., *Bourne and Willemse*, 2001]. Tensile fractures can occur at a range of depths (not just in the near surface) and predictive models which fail to account for tensile failure cannot be complete [e.g., *Maerten et al.*, 2002]. However, the problem in assigning failure mode to stress states derived from elastic models is illustrated by Figure 9b.

[29] This graph shows the total stress (ED + 50 m of overburden) states for all grid nodes in our Model 3a, expressed as maximum shear stress versus mean stress (both normalised by the cohesive strength, 1 MPa). Even with a reasonable failure criterion, e.g., with μ = 0.6, large parts of the modeled rock volume are predicted to have failed far in excess of the rock shear strength value. The problem then is to decide which failure mode, tensile or shear, the rock mass encountered first in moving from an initial unfractured stress state to its final fractured state. *Bourne and Willemse* [2001] approached this issue by calculating two measures of proximity to failure, one for tensile failure ($\chi_{tensile}$) and one for shear (χ_{shear}) failure (see Figure 9a). These values are calculated for the initial (preearthquake) and final (postearthquake) stress states, with negative values for χ below the failure envelope and positive values for χ above the envelope. The change in failure proximity for each failure mode is defined as:

$$\Delta\chi_{tensile} = \chi_{tensilefinal} - \chi_{tensileinitial} \quad (5)$$

$$\Delta\chi_{shear} = \chi_{shearfinal} - \chi_{shearinitial}. \quad (6)$$

The mode of first failure (if any) is then determined by the following conditions:

$$|\Delta\chi_{tensile}/\chi_{tensileinitial}| > |\Delta\chi_{shear}/\chi_{shearinitial}| \quad (7)$$

for tensile failure, and

$$|\Delta\chi_{shear}/\chi_{shearinitial}| > |\Delta\chi_{tensile}/\chi_{tensileinitial}| \quad (8)$$

for shear failure. Note that the conditions in (7) and (8) must use the absolute numerical values, as the initial χ

Table 3. Shear Failure Plane Classification Based on Orientation of Principal Stresses

Class	Criterion
Normal fault	σ_1 within 20° of vertical
Wrench fault	σ_2 within 20° of vertical
Reverse fault	σ_3 within 20° of vertical
Oblique-normal	σ_1 not within 20° of vertical, but σ_1 steepest
Oblique-wrench	σ_2 not within 20° of vertical, but σ_2 steepest
Oblique-reverse	σ_3 not within 20° of vertical, but σ_3 steepest

values in the denominators are usually negative (unfractured) and therefore the comparison is between two negative values.

[30] Given the mode of failure, we use a standard Coulomb failure criterion [e.g., *Jaeger and Cook*, 1979] to compute the angle of failure planes with respect to the principal axes of stress at each grid node. For tensile failure, fracture planes will be oriented parallel to the σ_1-σ_2 principal stress plane. For shear failure, conjugate failure planes intersecting parallel to σ_2 make an angle θ with σ_1 where

$$\theta = \pi/4 - \phi/2 \tag{9}$$

and ϕ is the angle of internal friction ($\tan\phi = \mu$). We further classify the shear failure planes on the basis of the orientation of their controlling principal stresses with respect to the free surface according to a simple Andersonian scheme [*Anderson*, 1951] described in Table 3. The predicted fracture maps shown in Figure 10 have all been constructed from a stress field comprising ED and overburden components only. For our preferred model (Model 3a), the majority of nodes where we predict failure involve the σ_2 principal stress oriented subhorizontally. In these cases, the map orientation (XY projection) of the σ_2 principal stress can be used as a proxy for the strike of failure planes, either tensile or shear.

[31] Figure 10 shows the distribution, mode and orientation of predicted fractures from Model 3a. The map in Figure 10a is a close-up of the area around panel 2 (south central segment of the fault system) and shows fractures at the surface (z = 0, no overburden stress). The strike of the predicted fractures is shown with a short line symbol. The strikes are parallel to σ_2 for tensile, normal and reverse fractures, whereas for wrench fractures (σ_2 vertical) the true strikes of the conjugate shear failure planes are shown. Areas with no symbols are predicted to remain intact. A range of fracture types (modes and orientations) is predicted at the surface, with tensile fractures dominant in a narrow (~1 km) zone in the hanging wall of panel 2. The tensile fractures strike broadly parallel to the underlying reverse fault. This predicted pattern closely matches the mapping of *Philip and Meghraoui* [1983] (their Figure 14; see also our Figure 1c). The effect of overburden stress is illustrated in Figure 10c which shows the same area as Figure 10a, but with predicted fractures at a depth of 50 m. Several oblique faults are now present, as the principal stress axes have rotated with increased distance from the free surface.

[32] Figure 10b illustrates the predicted fractures at the surface for the north central segment of the fault zone, around panel 3. Again the distribution and mode of predicted fractures corresponds closely to fractures in the field. However, the predicted strikes of the tensile fractures do not match the detailed mapping in this area by *Philip and Meghraoui* [1983] (their Figure 17; see also our Figure 1c). The strikes of the predicted fractures are not oblique to the main reverse fault trace (as observed), but subparallel to it. A similar pattern can be seen in the predicted fractures for a depth of 50 m, shown in Figure 10d. This shortcoming of the current model (Model 3a) is addressed further below.

5. Sensitivity Analysis

[33] Acknowledging that all forward models are nonunique, the main controls on the solution quality of ED models are the inputs e.g., regional stress (magnitude and direction), the chosen material parameters (elastic constants, rock strength values and friction), and the fault panel configuration (e.g., slip distribution). The predictions of our ED models are sensitive to the input material parameters. In this section we present maps of the stress field, at a depth of 50 m, to show the sensitivity to some of these parameters. The reference model for comparison with these parameter variations is shown in Figure 8f. A systematic sensitivity analysis allows us to explore other potential controls on fracture formation inherent within the geomechanical model.

5.1. Variations in the Regional Stress Field

[34] Although we believe the regional stress field exerts no obvious control on the formation of smaller scale fractures, we have explored the effect of varying the direction and magnitude of the regional stress. Figure 11a shows the combined ED, overburden and regional stress field based on a uniaxial regional shortening strain of 4.0×10^{-4} which is twice the amount suggested by *Ruegg et al.* [1982], at a depth of 50 m. The regional stress is now dominant with only very narrow zones of elastic perturbation around the fault panels (compare Figure 11a with Figure 8f). In contrast, halving the regional strain value to 1.0×10^{-4} (see Figure 11b) results in a combined stress field dominated by the coseismic elastic deformation around the faults.

[35] Another possible source of uncertainty is the azimuth of the uniaxial shortening. Our initial modeling (e.g., Figures 8e–8f) used a direction of 140°, consistent with many field observations by previous workers. Figure 11c shows a combined ED, overburden (50 m) and regional stress field based on a uniaxial shortening (at the original magnitude of 2.0×10^{-4}) aligned along 110°. The elastic stress perturbation in the near-field is manifest in the change in orientation of the principal stresses. While σ_2 around panel 2 (south central segment) remains subparallel to the fault trace, around panel 3 a slight obliquity is now

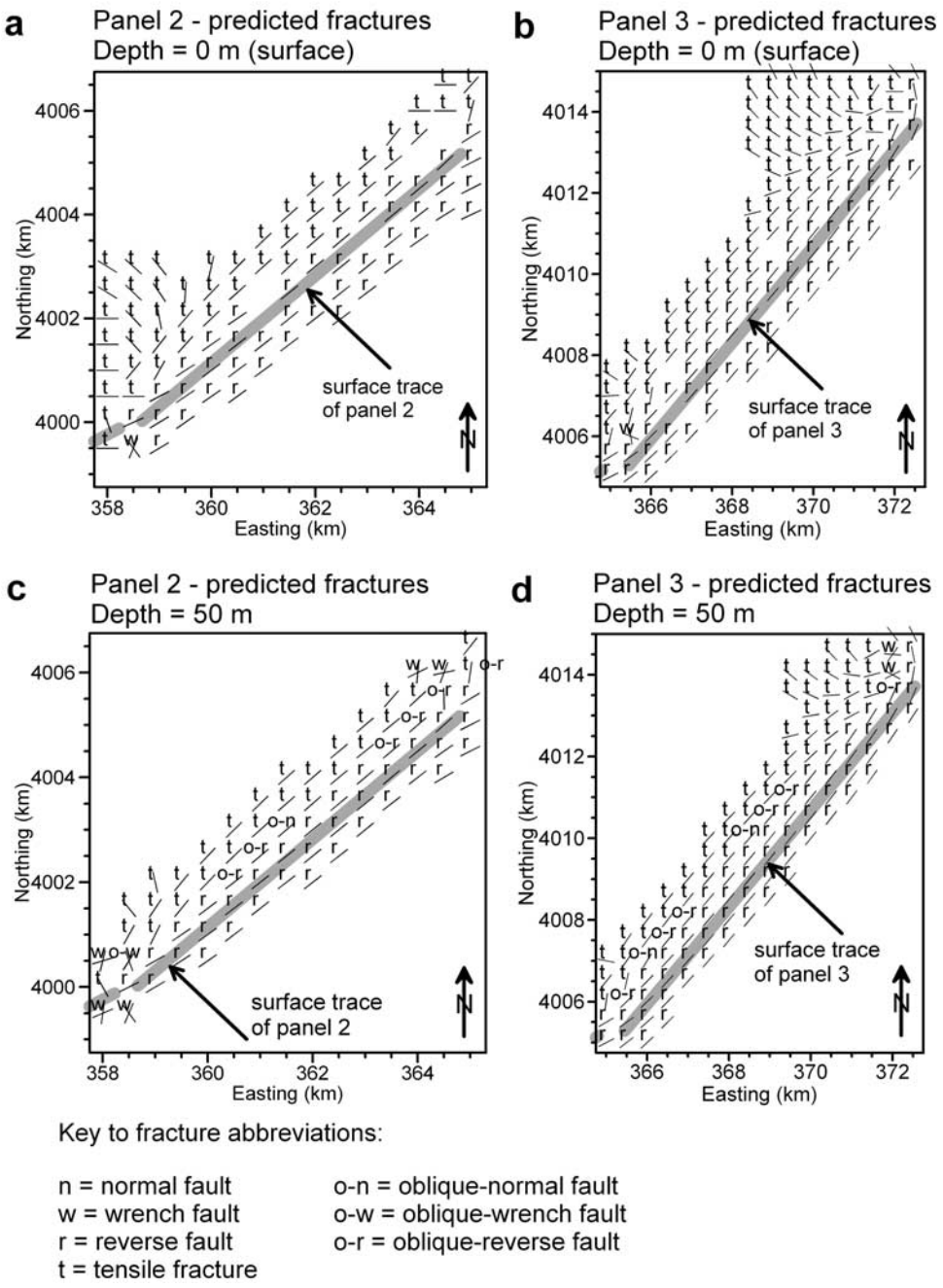

Figure 10. Maps of predicted fractures for Model 3a (pure reverse slip on all panels). Fractures are only shown at grid nodes where the rock is predicted to have failed according the χ test of *Bourne and Willemse* [2001]. (a) Map of predicted fractures around panel 2 derived from ED + overburden stresses at the surface (z = 0 m). (b) Map of predicted fractures around panel 3 derived from ED + overburden stresses at the surface (z = 0 m). (c) Map of predicted fractures around panel 2 derived from ED + overburden stresses in the subsurface (z = 50 m). (d) Map of predicted fractures around panel 3 derived from ED + overburden stresses in the subsurface (z = 50 m).

apparent. However, using these σ_2 directions as a proxy for fracture strike, the new orientations still do not match the NNE striking faults in this hanging wall. The overall plate convergence vector between Africa and Europe is around 170° [*Anderson and Jackson*, 1987], shown by the arrows on Figure 1a. Using this azimuth for the regional uniaxial shortening results in the combined stress field shown in Figure 11d. The near-field elastic perturbation is

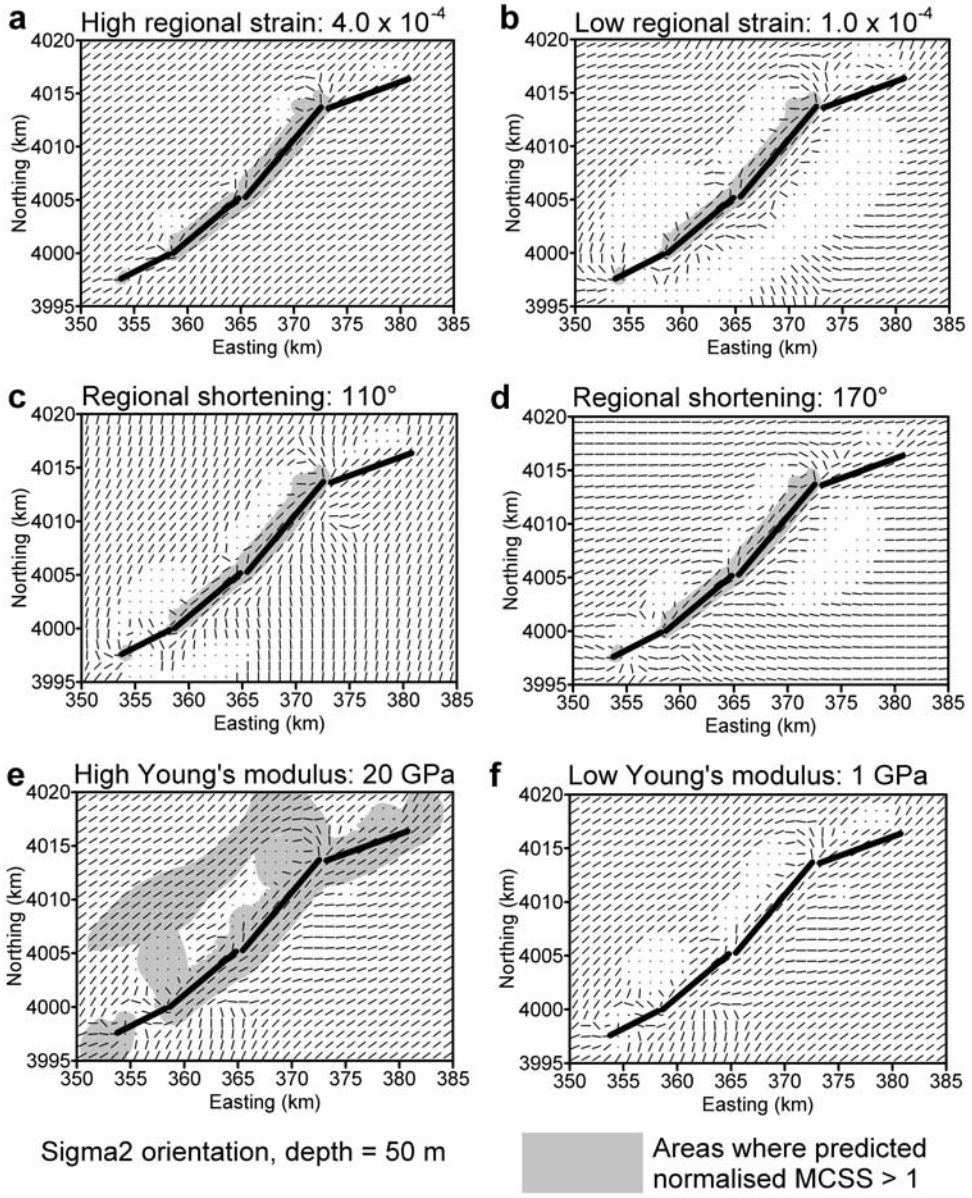

Figure 11. Sensitivity analysis. Maps show the orientations of σ_2 principal stress (intermediate) on a background of normalised maximum Coulomb shear stress for comparison with ''base case'' in Figure 8f. (a) ED + overburden + regional stresses in the subsurface (z = 50 m), based on a regional uniaxial strain value of 4.0×10^{-4}, i.e., twice the original amount. (b) ED + overburden + regional stresses in the subsurface (z = 50 m), based on a regional uniaxial strain value of 1.0×10^{-4}, i.e., half the original amount. (c) ED + overburden + regional stresses in the subsurface (z = 50 m), based on a regional uniaxial shortening direction of 110°, compared to the original direction of 140°. (d) ED + overburden + regional stresses in the subsurface (z = 50 m), based on a regional uniaxial shortening direction of 170°, compared to the original direction of 140°. (e) ED + overburden stresses in the subsurface (z = 50 m), using a higher value for Young's modulus of 20 GPa compared to the original value of 5 GPa. (f) ED + overburden stresses in the subsurface (z = 50 m), using a lower value for Young's modulus of 1 GPa compared to the original value of 5 GPa.

again apparent in the change in orientation of the principal stresses. In the hanging wall of panel 3, σ_2 is now slightly oblique to the underlying fault panel, rotated in a counterclockwise sense toward NNE. This is now more consistent with the normal faulting mapped along Sera el Maarouf. However, the obliquity is very slight and given our previous comments on the viability of a regional stress being sustained by these rocks, we discard this as an

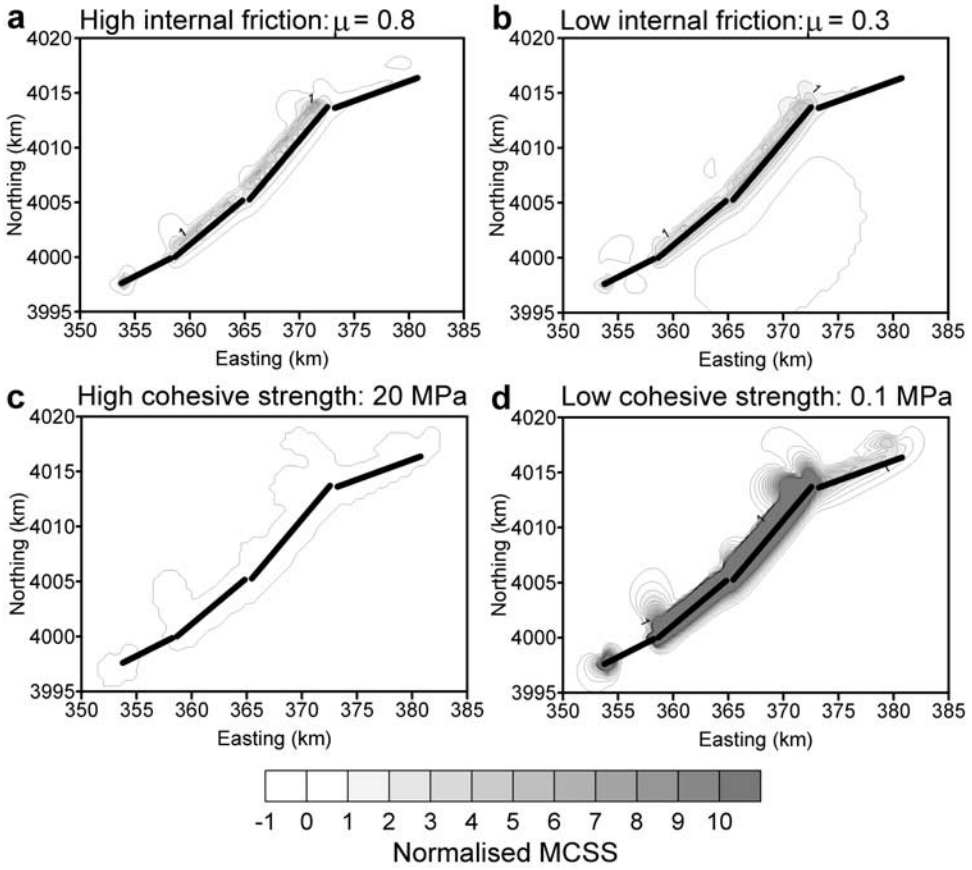

Figure 12. Sensitivity analysis. Maps of normalised maximum Coulomb shear stress. (a) ED + overburden stresses in the subsurface (z = 50 m), using a higher value for the coefficient of internal friction μ_i = 0.8 compared to the original value of μ_i = 0.6. (b) ED + overburden stresses in the subsurface (z = 50 m), using a lower value for the coefficient of internal friction μ_i = 0.3 compared to the original value of μ_i = 0.6. (c) ED + overburden stresses in the subsurface (z = 50 m), using a higher value for the cohesive strength of 20 MPa compared to the original value of 1 MPa. (d) ED + overburden stresses in the subsurface (z = 50 m), using a lower value for the cohesive strength of 0.1 MPa compared to the original value of 1 MPa.

explanation for the oblique NNE strike of these normal faults.

5.2. Variations in Material Parameters

[36] The Young's modulus (E) linearly scales the predicted strains and stresses and will affect the area and magnitude of predicted failure. Figure 11e shows the effect on the stress field of increasing E from an original value of 5 GPa, believed to be appropriate for these Neogene age sediments, to 20 GPa. The increased areal extent of normalised MCSS greater than 1 reflects this quadrupling of stress magnitude, with regions around the fault panels exceeding a normalised MCSS value of 5. Such areas are predicted to be intensely fractured or even brecciated, and this is not supported by the field evidence. Reducing the Young's modulus leads to a corresponding linear decrease in the stress magnitude, shown in Figure 11f for a value of 1 GPa. The maximum normalised MCSS value is now below 1, which would imply no new failure. Our original value of Young's modulus at 5 GPa appears valid.

[37] The coefficient of internal friction (μ) was initially set to 0.6, following *Byerlee* [1978]. In our model, the value of μ affects the distribution of fractures via the value of normalised MCSS (equation (4)). The orientation of conjugate shear failure planes about the principal compressive stress is also dependent on μ (equation (7)). Figures 12a and 12b show the effects of increasing μ to 0.8 and decreasing μ to 0.3, respectively. A higher value of μ leads to a slight increase in normalised MCSS, but neither map shows any marked difference from the basic model in Figure 8. Our model is therefore not particularly sensitive to changes in μ, and we prefer the original value of 0.6.

[38] Finally, we consider the values for rock strength. Our original value (see Table 1) for the tensile strength (T_0) was 0.5 MPa, with the shear strength (C) set at 1 MPa. These

parameters are used to determine the proximity to failure and will therefore affect both the mode (i.e., tensile or shear) and distribution of the predicted fractures. A higher tensile strength of 10 MPa, with a corresponding increase of shear strength to 20 MPa, results in low values of normalised MCSS (see Figure 12c) i.e., a prediction of a very low degree of fracturing. By comparison, reducing T_0 to 0.05 MPa (and C to 0.1 MPa) leads to a significant increase in normalised MCSS, a prediction of intense fracturing or brecciation (Figure 12d). Neither case seems warranted by the field evidence, and we believe the initial value for T_0 of 0.5 MPa is more appropriate.

5.3. Variations in Slip Distribution

[39] As discussed above, our initial model (Model 3a) fails to predict the oblique strikes (NNE) of the normal faults in the hanging wall of the north central segment. We now explore the control of the prescribed slip distribution on the predicted stress field and fracture pattern. Our initial model 3a (see Table 2) specifies uniform reverse slip values on the three subpanels 3a, b and c. An alternative scenario might involve a lateral (i.e., along strike) variation in slip on these subpanels. Figures 13a–13b shows the predicted stress field using the slip values listed in Table 4, with a northeastward decrease in reverse slip. The normalised MCSS now decreases toward the NE, suggesting less intense fracturing at the NE tip. The most compressive stress σ_1 is oriented subvertically along the high stress zone, consistent with extensional fractures. However, the orientation of σ_2 (proxy for fault strike) in the hanging wall remains subparallel to the reverse fault panel. Model 3b therefore also fails to predict the NNE trending normal faults.

[40] There is some dispute as to the role of sinistral slip in the 1980 event. Field evidence [*Philip and Meghraoui*, 1983] has been interpreted as a significant component (of the order of meters) of sinistral slip in producing the mapped surface breaks. Previous elastic dislocation models [*Ruegg et al.*, 1982; *Cisternas et al.*, 1982] have also used a sinistral slip component to achieve a fit between observed and modeled vertical displacements. *Philip and Meghraoui* [1983] propose a model (their Figure 41) involving oblique sinistral-reverse slip on the north central fault segment to account for the NNE trending normal faults in the hanging wall. Over many earthquake cycles, the plate convergence direction of 170° will probably lead to oblique slip on faults striking 050°. However, the primary field observations along Sera el Maarouf from *Yielding et al.* [1981] (their Figure 4) clearly show that the slip vectors on the NNE trending normal faults are parallel to the main reverse fault slip vector, i.e., along 140°. In addition, these normal faults were in existence before the 1980 earthquake, and have been reactivated by that event. Therefore the stress field responsible for the initiation of these fractures need not be the same as that of the 1980 event.

[41] A feature of our preferred model thus far (Model 3a) is the sharp decrease in reverse slip values near the surface. The shallowest panels (2c and 3c, see Table 2) in the central segment are narrow in a downdip direction and carry only minor reverse slip values. This configuration produces the narrow linear zones of uplift and high ED strain in the immediate hanging walls of the panels 2 and 3. One interpretation of this geometry is that it is an upward propagating reverse fault tip that has recently breached the surface. At some time before the 1980 earthquake, the tip line of the reverse fault system in this segment would have been blind i.e., subsurface. In our final model (Model 3c, see Table 5), panel 3c has been removed and the upper edge of panel 3b now represents the buried tip line, 0.7 km deep, of the reverse fault system. In addition, a small (3 m) sinistral slip component has been added to panel 3b. This results in oblique (sinistral-reverse) slip on this panel, with a slip vector azimuth of 153° (as opposed to 130° on the original pure reverse slip model 3a). The consequences of oblique slip on buried dislocations in an elasto-plastic medium have recently been described by *Bowman et al.* [2003]. Model 3c confirms their findings that complex yet systematic strain and stress patterns develop in the volume above the buried fault. Figures 13c–13d shows the stress field at a depth of 50 m with a blind panel 3 (tip-line buried 0.71 km) and oblique sinistral-reverse slip. A narrow linear zone of high stress is present in the hanging wall and σ_1 is again subvertical in this region. The small sinistral component of slip has a significant effect on the orientation of σ_2, which now trends NNE in a narrow zone approximately 1–2 km behind the projected surface fault trace. Employing σ_2 as a proxy for fault strike, this model can account for the en echelon NNE striking normal faults observed along Sera el Maarouf.

[42] Changing the slip distribution will also impact the predicted vertical displacement field. Figure 14 shows contour maps of the vertical displacement at the surface for the region around panel 3 (north central segment) for each of the models 3a, b and c. The northeastward decrease in reverse slip in model 3b results in a tapering of the linear uplifted zone in the hanging wall (Figure 14b). Repeated slip events of this type would result in an anticline plunging moderately to the NE, which is far in excess of the slight plunge observed. The oblique slip in model 3c maintains a large amount of uplift along the whole length of the hanging wall of panel 3 (Figure 14c). One or more previous, pre-1980, events involving oblique sinistral-reverse slip can account for the NNE trending normal faults along Sera el Maarouf, which were then reactivated during the 1980 reverse slip event. Figures 15a–15c show the predicted fractures for the pre-1980 oblique slip event, at the surface, at 50 m and at 100 m depth, respectively. NNE trending tensile fractures and oblique normal faults dominate, interspersed with wrench and other oblique fault combinations above the blind fault tip-line. For comparison with the field data, Figure 15d is a structural map of surface fractures along Sera el Maarouf taken from *Philip and Meghraoui* [1983] (their Figure 17).

6. Discussion

[43] The role of pore-fluid pressure has not been considered in our modeling, but there is significant field evidence

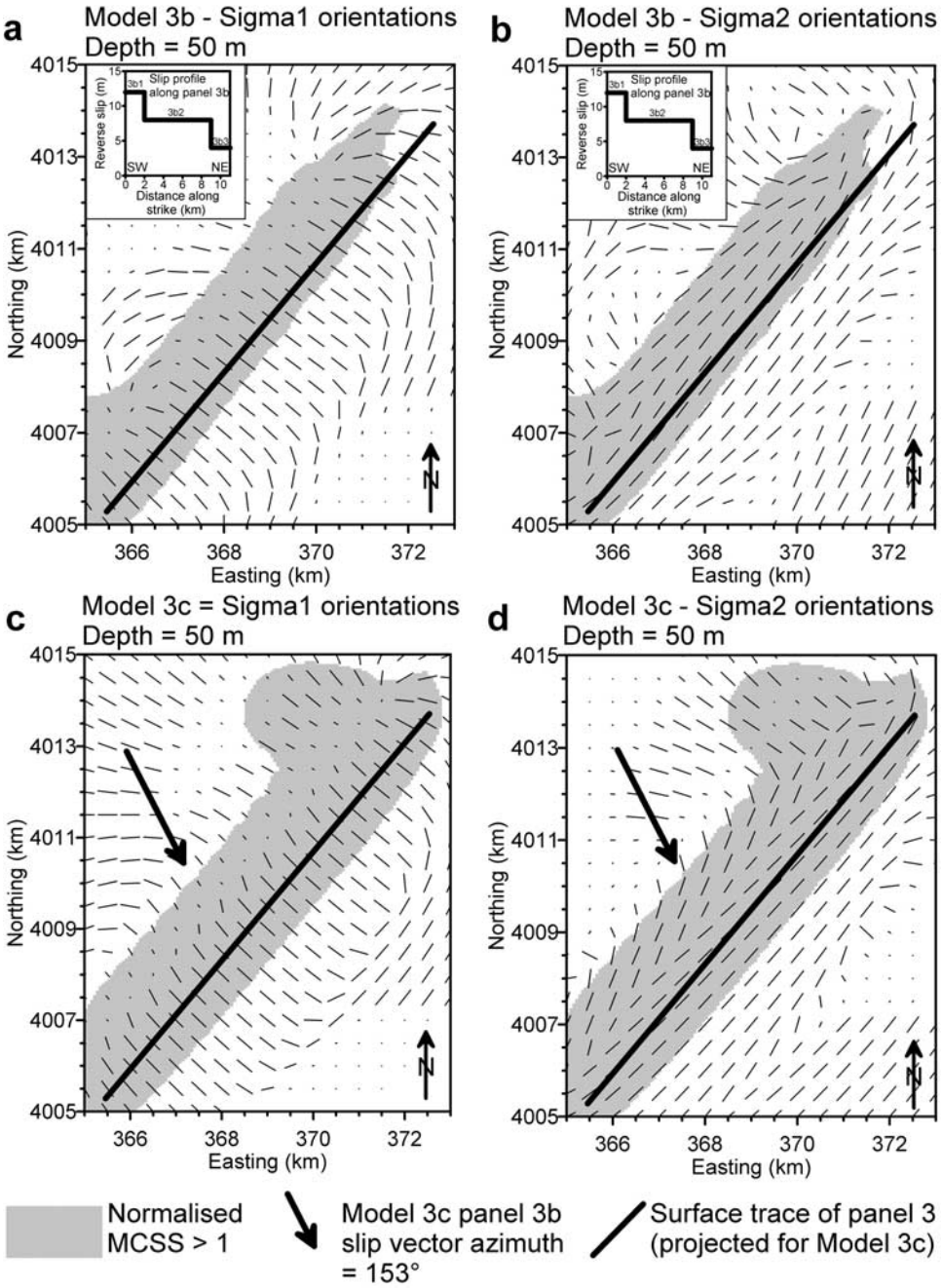

Figure 13. (a) Map of ED + overburden stresses in the subsurface (z = 50 m) for Model 3b, with a lateral slip gradient on the subpanels of panel 3. Slip decreases to the NE (see Table 4). Orientations of σ_1 principal stress (most compressive) on a background of normalised maximum Coulomb shear stress. (b) Orientations of σ_2 principal stress (intermediate) for Model 3b on a background of normalised maximum Coulomb shear stress. (c) Map of ED + overburden stresses in the subsurface (z = 50 m) for Model 3c, with sinistral reverse slip on the subpanels of panel 3 (see Table 5). In addition, panel 3 does not breach the surface in this model. Orientations of σ_1 principal stress (most compressive) on a background of normalised maximum Coulomb shear stress. (d) Orientations of σ_2 principal stress (intermediate) for Model 3c on a background of normalised maximum Coulomb shear stress.

Table 4. Fault Panel Data for the Model 3b Illustrated in Figures 13 and 14[a]

	UTM Coordinates (Zone 31), km			Dimensions, km		Orientation, deg		Fault Slip, m	
Panel	X	Y	Z	L	W	Dip	Strike	Sinistral	Reverse
1	353.33	4003.99	8.09	5.0	10.00	54.0	063	0.0	4.0
2a	357.77	4007.33	8.49	8.0	4.25	54.0	050	0.0	6.5
2b	359.37	4005.41	5.06	8.0	5.50	54.0	050	0.0	9.0
2c	361.45	4002.94	0.61	8.0	0.75	54.0	050	0.0	1.0
3a1	360.69	4010.60	7.07	2.0	4.00	45.0	040	0.0	5.5
3b1	362.86	4008.78	4.24	2.0	5.00	45.0	040	0.0	12.0
3c1	365.57	4006.50	0.71	2.0	1.00	45.0	040	0.0	0.6
3a2	363.58	4014.05	7.07	7.0	4.00	45.0	040	0.0	4.0
3b2	365.75	4012.23	4.24	7.0	5.00	45.0	040	0.0	8.0
3c2	368.46	4009.95	0.71	7.0	1.00	45.0	040	0.0	0.6
3a3	366.47	4017.50	7.07	2.0	4.00	45.0	040	0.0	2.0
3b3	368.64	4015.68	4.24	2.0	5.00	45.0	040	0.0	4.0
3c3	371.35	4013.40	0.71	2.0	1.00	45.0	040	0.0	0.6
4	373.88	4023.70	7.72	8.0	10.00	40.0	070	0.0	3.0

[a]Panels from Model 3a (see Table 2, Model 3c data) have been modified to include more subpanels and a slip gradient. Reverse dip-slip values decrease to the NE.

for fluid activity, e.g., sand craterlets appeared in the footwall of the north central segment after the 1980 event. However, there is no field evidence for significant fluid activity in the fractures exposed at the surface, and we retain the simplifying assumption of no pore-fluid pressure (see also comment on p.8) Our models make no predictions regarding the size of the fractures. Some of the mapped ''minor'' faults are now up to 1 km long, and presumably have grown through many seismic cycles. The lack of any fracture dimensions in the model output remains a limitation, which could be addressed by using our results as input to discrete fracture modeling [e.g., *Maerten et al.*, 2004].

7. Summary

[44] Forward modeling based on ED theory can predict the distribution of small-scale fractures around larger faults. In contrast to stochastic fault scaling methods, geomechanical models based on ED theory predict the spatial distribution of small-scale fractures. The orientation of failure planes can only be accurately predicted once the failure mode (tensile or shear) has been determined. For the ED models presented, much of the rock volume has far exceeded conservative estimates of the failure envelope and the determination of failure mode is achieved through the method of *Bourne and Willemse* [2001]. A complex distribution of different fracture modes, fault types and orientations has been described by previous workers around El Asnam. We have shown how the predictions from simple ED models can be tested against these detailed field observations. For example, a pure reverse slip model fails to predict the NNE trending normal faults in the hanging wall along Sera el Maarouf. However, a previous (pre-1980) increment of oblique sinistral-reverse slip on a blind upward propagating fault panel can account for these surface fractures. The modeling technique presented in this paper, although simple, can predict the full range of observed fracture styles and orientations. The overall agreement between predicted and observed fractures lends confidence in the use of ED models in accurately predicting the complex deformation represented by secondary fractures around larger faults.

Table 5. Fault Panel Data for the Model 3c Illustrated in Figures 13, 14, and 15[a]

	UTM Coordinates (Zone 31), km			Dimensions, km		Orientation, deg		Fault Slip, m	
Panel	X	Y	Z	L	W	Dip	Strike	Sinistral	Reverse
1	353.33	4003.99	8.09	5.0	10.00	54.0	063	0.0	4.0
2a	357.77	4007.33	8.49	8.0	4.25	54.0	050	0.0	6.5
2b	359.37	4005.41	5.06	8.0	5.50	54.0	050	0.0	9.0
2c	361.45	4002.94	0.61	8.0	0.75	54.0	050	0.0	1.0
3a	363.58	4014.05	7.07	11.0	4.00	45.0	040	0.0	5.5
3b	365.75	4012.23	4.24	11.0	5.00	45.0	040	3.0	12.0
4	373.88	4023.70	7.72	8.0	10.00	40.0	070	0.0	3.0

[a]Panel 3 from Model 3a (see Table 2c) has been modified to include a component of sinistral strike-slip: 3 m on subpanel 3b. The combination of sinistral and reverse slip components results in an oblique slip vector trending 153° (compare with Model 3a where the reverse slip vector trends 130°). Note also that subpanel 3c has been removed from this model, and therefore panel 3 now represents a blind fault with a tip line 710 m below the surface.

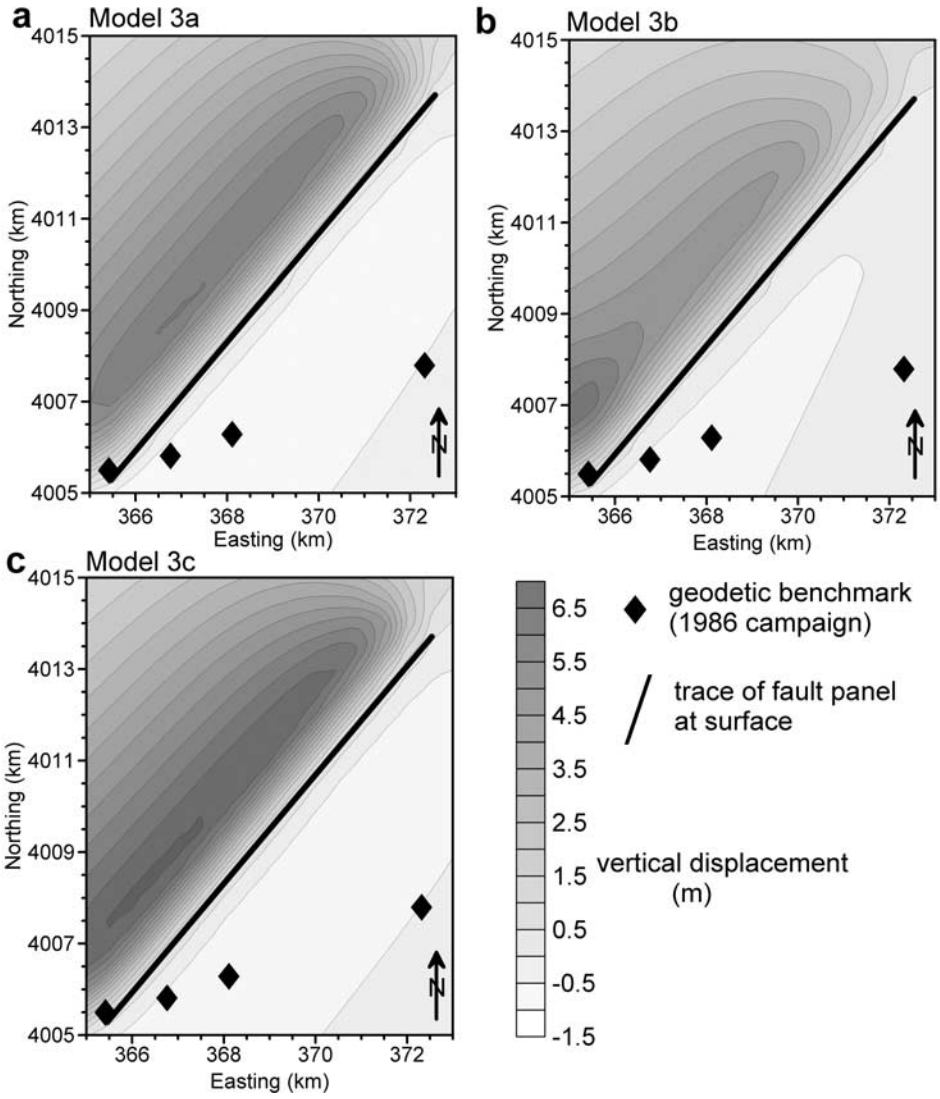

Figure 14. Maps of calculated vertical displacement ($\mathbf{u}_z$ component of elastic displacement field) at the surface ($z = 0$ m) for Models 3a, b and c, contoured in meters. (a) Close-up map of vertical displacement around panel 3 in Model 3a. The narrow linear zone of uplift in the hanging wall matches the location of the anticline along Sera el Maarouf. (b) Model 3b has a gradient of reverse slip on panel 3, with slip decreasing to the NE (see Table 4). This slip distribution produces a corresponding northeastward decrease in uplift in the hanging wall of panel 3. Successive similar slip increments would therefore result in a definite NE plunge to the hanging wall anticline, far in excess of the slight plunge observed. (c) Model 3c (see Table 5) with a small (3 m) component of sinistral slip in addition to reverse slip. The uplifted ridge in the hanging wall is more elongated than in Model 3b, and tapers gently toward the NE. This is more consistent with the topography observed in the field.

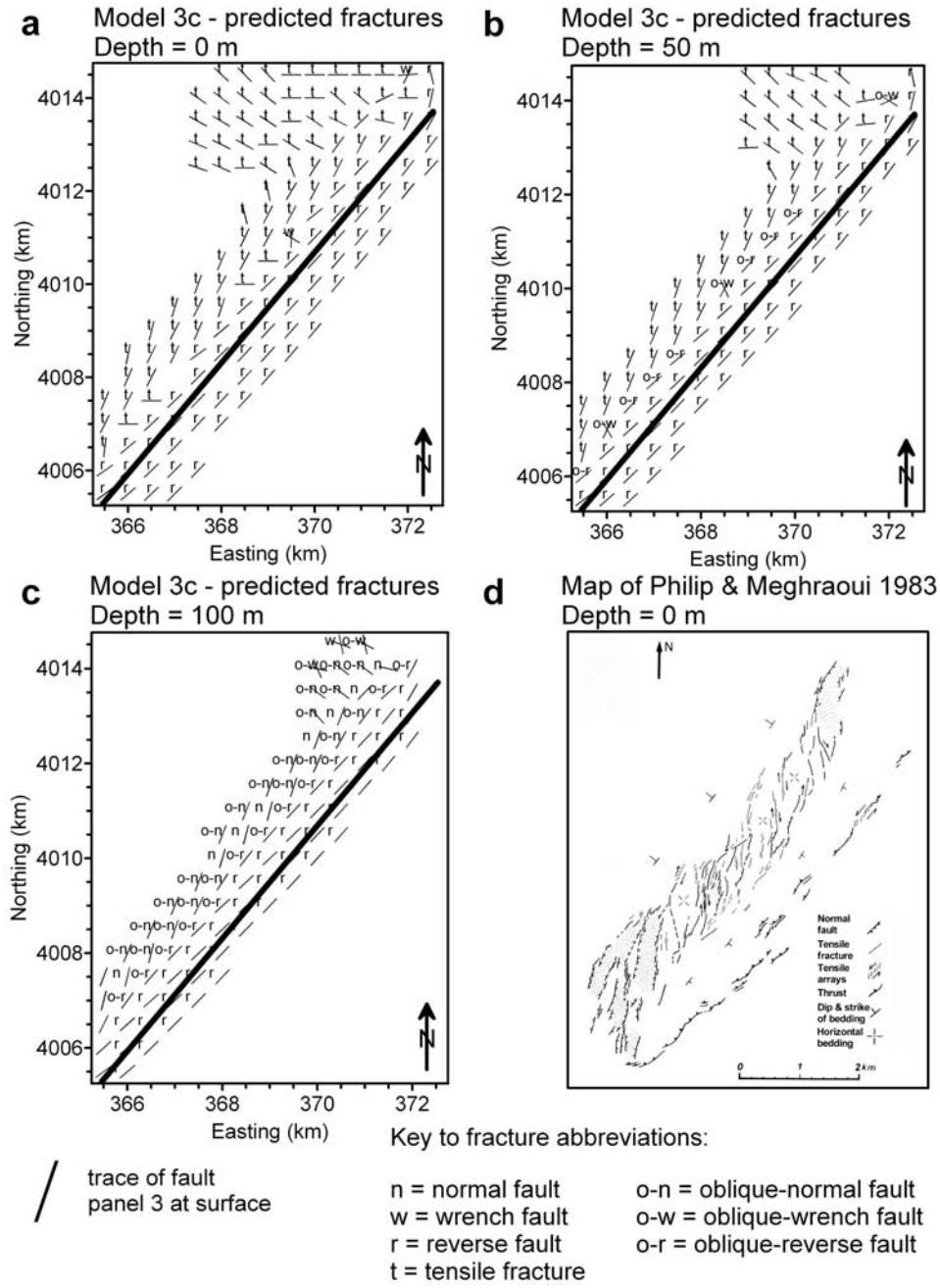

Figure 15. Maps of predicted fractures around panel 3 for Model 3c, with oblique sinistral-reverse slip on panel 3b. Fractures are only shown at grid nodes where the normalised maximum Coulomb shear stress exceeds 1, i.e., where the rock is predicted to have failed. Note that panel 3 does not breach the surface in this model; the bold gray line marks the projected surface trace of the buried tip line. (a) Fractures derived from ED + overburden stresses at the surface (z = 0 m). (b) Fractures derived from ED + overburden stresses in the subsurface at a depth of 50 m. (c) Fractures derived from ED + overburden stresses in the subsurface at a depth of 100 m. For comparison with the fractures predicted by our model, Figure 15d shows a geological map of surface fractures produced by *Philip and Meghraoui* [1983] (their Figure 17), covering the same area as shown in Figures 15a–15c.

[45] **Acknowledgments.** This work was funded by EPSRC/DTI grant GR/N20287/01, which is gratefully acknowledged. David Healy would like to thank the Department of Earth and Ocean Sciences, University of Liverpool for assistance with Ph.D. research funding. Thanks also to Mike Badley, Brett Freeman, Stephen Dee, and Ken Baxter, all at Badleys. The original manuscript was substantially improved thanks to constructive reviews by Geoff King (Institut de Physique du Globe, Paris) and an anonymous reviewer, and from the editorial assistance of Brian Wernicke.

References

Anderson, E. M. (1951), *The Dynamics of Faulting and Dyke Formation With Application to Britain*, 2nd ed., Oliver and Boyd, Edinburgh.

Anderson, H., and J. Jackson (1987), Active tectonics of the Adriatic region, *Geophys. J. R. Astron. Soc.*, *91*, 937–983.

Bezzeghoud, M., D. Dimitrov, J. C. Ruegg, and K. Lammali (1995), Faulting mechanism of the El Asnam (Algeria) 1954 and 1980 earthquakes from modelling of vertical movements, *Tectonophysics*, *249*, 249–266.

Bourne, S. J., and E. J. M. Willemse (2001), Elastic stress control on the pattern of tensile fracturing around a small fault network at Nash Point, UK, *J. Struct. Geol.*, *23*, 1753–1770.

Bourne, S. J., L. Rijkels, B. J. Stephenson, and E. J. M. Willemse (2001), Predictive modelling of naturally fractured reservoirs using geomechanics and flow simulation, *GeoArabia*, *6*, 27–41.

Bowman, D. D., G. C. P. King, and P. Tapponnier (2003), Slip partitioning by elasto-plastic propagation of oblique slip at depth, *Science*, *300*, 1121–1123.

Brustle, W., and G. Muller (1983), Moment and duration of shallow earthquakes from Love-wave modelling for regional distances, *Phys. Earth Planet. Inter.*, *32*, 312–324.

Byerlee, J. (1978), Friction of rocks, *Pure Appl. Geophys.*, *116*, 615–626.

Cisternas, A., J. Dorel, and R. Gaulon (1982), Models of the complex source of the El Asnam earthquake, *Bull. Seismol. Soc. Am.*, *72*, 2245–2266.

Deschamps, A., Y. Gaudemer, and A. Cisternas (1982), The El Asnam, Algeria, earthquake of 10 October 1980: Multiple-source mechanism determined from long-periods, *Bull. Seismol. Soc. Am.*, *72*, 1111–1128.

Jaeger, J. C., and N. G. W. Cook (1979), *Fundamentals of Rock Mechanics*, 585 pp., Chapman and Hall, New York.

King, G. C. P., and C. Vita-Finzi (1981), Active folding in the Algerian earthquake of 10 October 1980, *Nature*, *292*, 22–26.

King, G. C. P., and G. Yielding (1984), The evolution of a thrust fault system: Processes of rupture initiation, propagation and termination in the 1980 El Asnam (Algeria) earthquake, *Geophys. J. R. Astron. Soc.*, *77*, 915–933.

Maerten, L., P. Gillespie, and D. D. Pollard (2002), Effects of local stress perturbation on secondary fault development, *J. Struct. Geol.*, *24*, 145–153.

Maerten, L., P. Gillespie, and J.-M. Daniel (2004), 3-D geomechanical modelling for constraint of subseismic fault simulation, *AAPG Mem.*, in press.

Okada, Y. (1985), Surface deformation due to shear and tensile faults in a half-space, *Bull. Seismol. Soc. Am.*, *75*, 1135–1154.

Okada, Y. (1992), Internal deformation due to shear and tensile faults in a half-space, *Bull. Seismol. Soc. Am.*, *82*, 1018–1040.

Philip, H., and M. Meghraoui (1983), Structural analysis and interpretation of the surface deformations of the El Asnam earthquake of October 10, 1980, *Tectonics*, *2*, 17–49.

Rongved, L., and J. T. Frasier (1958), Displacement discontinuity in the elastic half-space, *J. Appl. Mech.*, *25*, 125–128.

Ruegg, J. C., M. Kasser, A. Tarantola, J. C. Lepine, and B. Chouikrat (1982), Deformations associated with the El Asnam earthquake of 10 October 1980: Geodetic determination of vertical and horizontal movements, *Bull. Seismol. Soc. Am.*, *72*, 2227–2244.

Stein, R. S., and S. E. Barrientos (1985), Planar high-angle faulting in the Basin and Range: Geodetic analysis of the 1983 Borah Peak, Idaho, earthquake, *J. Geophys. Res.*, *90*, 11,355–11,366.

Stein, R. S., G. C. P. King, and J. B. Rundle (1988), The growth of geological structures by repeated earthquakes: 2. Field examples of continental dip-slip faults, *J. Geophys. Res.*, *93*, 13,319–13,331.

Steketee, J. A. (1958), Some geophysical applications of the elasticity theory of dislocations, *Can. J. Phys.*, *36*, 1168–1198.

Vita-Finzi, C., and G. C. P. King (1985), The seismicity, geomorphology and structural evolution of the Corinth area of Greece, *Philos. Trans. R. Soc. London, Ser. A*, *314*, 379–407.

Yielding, G. (1985), Control of rupture by fault geometry during the 1980 El Asnam (Algeria) earthquake, *Geophys. J. R. Astron. Soc.*, *81*, 641–670.

Yielding, G., J. A. Jackson, G. C. P. King, H. Sinvhal, C. Vita-Finzi, and R. M. Wood (1981), Relations between surface deformation, fault geometry, seismicity, and rupture characteristics during the El Asnam (Algeria) earthquake of 10 October 1980, *Earth Planet. Sci. Lett.*, *56*, 287–304.

Yielding, G., M. Ouyed, G. C. P. King, and D. Hatzfeld (1989), Active tectonics of the Algerian Atlas Mountains—Evidence from aftershocks of the 1980 El-Asnam earthquake, *Geophys. J. Int.*, *99*, 761–788.

D. Healy and N. Kusznir, Department of Earth and Ocean Sciences, University of Liverpool, Liverpool L69 3GP, UK. (dhealy@liverpool.ac.uk)

G. Yielding, Badleys, North Beck House, North Beck Lane, Hundleby, Spilsby, Lincolnshire PE23 5NB, UK.